MACS J0553.4−3342: a young merging galaxy cluster caught through the eyes of *Chandra* and *HST*

M. B. Pandge,[1][*] Joydeep Bagchi,[2] S. S. Sonkamble,[3] Viral Parekh,[4] M. K. Patil,[3] Pratik Dabhade,[2] Nilam R. Navale,[1] Somak Raychaudhury[2,5] and Joe Jacob[6]

[1]*DST INSPIRE Faculty, Dayanand Science College, Barshi Road, Latur 413512, Maharashtra, India*
[2]*Inter-University Centre for Astronomy and Astrophysics, Post Bag 4, Ganeshkhind, Puné 411007, India*
[3]*School of Physical Sciences, Swami Ramanand Teerth Marathwada University, Nanded 431606, India*
[4]*Raman Research Institute, C. V. Raman Avenue, Sadashivnagar, Bengaluru 560080, India*
[5]*Department of Physics, Presidency University, 86/1 College Street, Kolkata 700073, India*
[6]*Newman College, Thodupuzha, Kerala, 685584, India*

ABSTRACT

We present a detailed analysis of a young merging galaxy cluster MACS J0553.4−3342 (z=0.43) from *Chandra* X-ray and *Hubble Space Telescope* archival data. X-ray observations confirm that the X-ray emitting intra-cluster medium (ICM) in this system is among the hottest (average $T = 12.1 \pm 0.6\,\mathrm{keV}$) and most luminous known. Comparison of X-ray and optical images confirms that this system hosts two merging subclusters SC1 and SC2, separated by a projected distance of about 650 kpc. The subcluster SC2 is newly identified in this work, while another subcluster (SC0), previously thought to be a part of this merging system, is shown to be possibly a foreground object. Apart from two subclusters, we find a tail-like structure in the X-ray image, extending to a projected distance of ∼1 Mpc, along the north-east direction of the eastern subcluster (SC1). From a surface brightness analysis, we detect two sharp surface brightness edges at ∼40 (∼320 kpc) and ∼80 arcsec (∼640 kpc) to the east of SC1. The inner edge appears to be associated with a merger-driven cold front, while the outer one is likely to be due to a shock front, the presence of which, ahead of the cold front, makes this dynamically disturbed cluster interesting. Nearly all the early-type galaxies belonging to the two subclusters, including their brightest cluster galaxies, are part of a well-defined red sequence.

Key words: galaxies: active – galaxies: clusters: individual: MACS J0553.4−3342 – galaxies: general – X-rays: galaxies: clusters.

1 INTRODUCTION

Galaxy clusters are among the most massive gravitationally bound systems in the Universe, assembled from the hierarchical merging of smaller sub-haloes over cosmic time. Evidence of such interactions among the smaller systems remain in present-day clusters in the form of subclustering in the distribution of galaxies, and in the hot intra-cluster medium (ICM) in the form of cold fronts, shock heating (Markevitch & Vikhlinin 2007; Plagge et al. 2010), turbulence and substructure (Ogrean et al. 2015; Botteon et al. 2016; Dasadia et al. 2016). Signatures of such mergers can also be observed as diffuse non-thermal synchrotron radio emission in the form of radio haloes and relics (e.g. Bagchi et al. 2002, 2006, 2011; Bonafede et al. 2012; Feretti et al. 2012). Cluster mergers provide

ideal settings for detailed studies to understand important aspects of the physical processes involved in these mergers, including the thermodynamics of the hot gas, magnetic field amplification and high-energy particle acceleration (cosmic rays) by shocks and turbulence (Randall et al. 2008; van Weeren et al. 2009; Bonafede et al. 2012; ZuHone et al. 2015), and offsets between the gas and the dark matter (DM) subclusters.

In this paper, we present the results from the analysis of an 83 ks *Chandra* X-ray observation, along with archived *Hubble Space Telescope* (*HST*) optical observations of the extremely hot, massive and X-ray luminous merging galaxy cluster MACS J0553.4−3342 (z=0.43; Mann & Ebeling 2012). X-ray and radio studies of this cluster have been reported earlier by Mann & Ebeling (2012) and Bonafede et al. (2012), using the shallower *Chandra* (9.86 ks) and Giant Metrewave Radiotelescope (GMRT) observations, respectively, where a disturbed X-ray structure and a radio halo extending over

[*] E-mail: mbpandge@gmail.com

Table 1. *Chandra* observation log for MACS J0553.4−3342.

Obs ID	Observing mode	CCDs on	Starting date	Total time (ks)	Clean time (ks)
12244	VFAINT	0,1,2,3,6	2011-06-23	74.06	73.28
5813	VFAINT	0,1,2,3,6	2005-01-08	9.94	9.86

∼1.3 Mpc scale have been reported. The joint X-ray and optical study presented in Mann & Ebeling (2012) pointed out that this system appears to result from an ongoing merger of two subclusters of similar mass. We present below a detailed morphological and thermodynamical analysis of the distribution of the ICM in this system. This paper also investigates the evidence for shock and cold fronts, to better understand the merger scenario in this system.

The structure of this paper is as follows. In Section 2, we describe the X-ray data reduction and imaging. Section 3 represents an optical analysis, including an optical identification of the subclusters, and a colour–magnitude diagram (CMD) of the subcluster. Section 4 presents the spatial and spectral analyses of the X-ray data, including surface brightness profiles, and the spatial variation of the temperature of the ICM in the form of a two-dimensional map. Results derived from the present study are discussed in Section 4, while Section 5 describes the main conclusions of the study. Throughout this paper, we assume Λ cold dark matter cosmology with $H_0 = 73 \text{ km s}^{-1} \text{ Mpc}^{-1}$, $\Omega_M = 0.27$ and $\Omega_\Lambda = 0.73$, translating to a scale of 8.091 kpc arcsec^{-1} at the redshift $z = 0.43$ of MACS J0553.4−3342. All spectral analysis uncertainties are reported at the 90 per cent confidence level, while all other uncertainties are given at 68 per cent confidence level.

2 X-RAY DATA REDUCTION AND IMAGING

MACS J0553.4−3342 has been observed twice by the *Chandra* X-ray Observatory, once in 2005 January and later in 2011 June, for an effective combined exposure of 83 ks (Obs ID 5813 and 12244; for details see Table 1). Both the observations were reprocessed using the CHANDRA_REPRO task available within CIAO[1] 4.8, employing the recent calibration files CALDB 4.7.2 provided by the *Chandra* X-ray Centre (CXC). We followed the standard *Chandra* data reduction threads[2] for the analysis of these observations. Periods of high-background flares exceeding 20 per cent of the mean background count rates were identified and removed from further analysis using the *lc_sigma_clip* algorithm. We used the CIAO REPROJECT_OBS task to reproject the event files and the exposure maps in the energy range 0.7−7.0 keV, creating exposure-corrected images with the FLUX_OBS script.

The ACIS_BKGRND_LOOKUP script within CIAO was used to identify the suitable blank sky background fields corresponding to each of the event files. The X-ray background files were modelled using the 'blank sky' data sets, and were reduced following the standard procedure outlined in http://cxc.harvard.edu/contrib/maxim/acisbg. We reprojected these sky background fields to match the coordinates of the observations and scaled them appropriately so that their hard band (9−12 keV) count rates matched those in the science frames before subtraction.

Point sources identified from the resultant image using the WAVDETECT algorithm were excluded from the subsequent analysis. For the spectral analysis of the ICM, selected from different
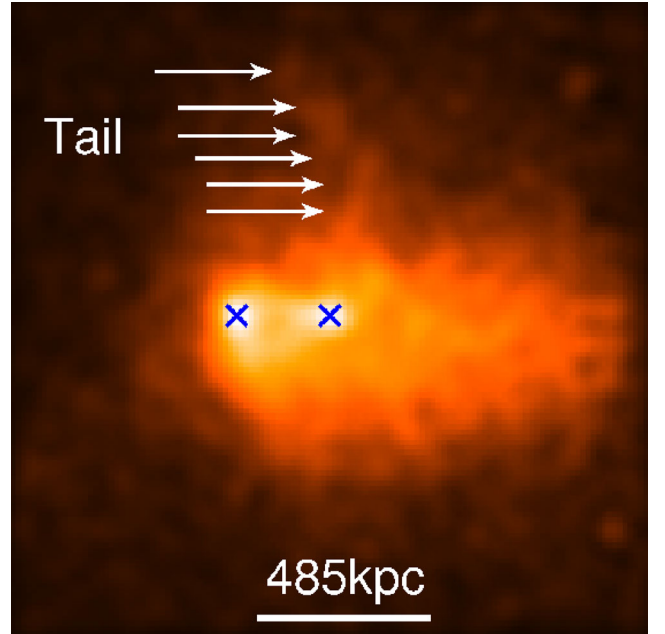
Figure 1. Background-subtracted, exposure-corrected central 5 × 5 arcmin^2 *Chandra* image (0.7–2.0 keV) of MACS J0553.4−3342. This image has been smoothed with a Gaussian kernel of width $\sigma = 3$ arcsec. Arrows in this figure indicate the presence of an X-ray tail-like feature, seen along the north-east direction, appearing to originate from the centre of eastern subcluster (SC1). The two subclusters identified by Mann & Ebeling (2012) are highlighted by blue crosses.

regions of interest, we generated corresponding Redistribution Matrix Files (RMF), Ancillary Response Files (ARF) using the task SPECEXTRACT available within CIAO. These spectra were then exported to XSPEC (version 12.9.1, Arnaud 1996) for further analysis. The exposure-corrected, background-subtracted, 0.7−2.0 keV *Chandra* image of the central 5 × 5 arcmin^2 region of MACS J0553.4−3342 is shown in Fig. 1. The blue crosses in this figure indicate the positions of the two previously identified subclusters (SC0 and SC1) (Mann & Ebeling 2012).

3 OPTICAL ANALYSIS

3.1 Optical identification of the subclusters

To investigate the nature of optical counterparts of the two possible subclusters SC0 and SC1 (Bonafede et al. 2012), associated with the two peaks of X-ray emission (shown by the blue crosses in Fig. 1), we used the three broad-band imaging observations of MACS J0553.4−3342, taken in filters F435W (*B*), F606W (*V*) and F814W (*I*), with effective exposure times of 4572 s, 2092 s and 4452 s, respectively, from the *HST* archives. Among these, we use the F814W image for finding optical counterparts of the possible subclusters. We created a tri-colour map by combining the optical F814W (shown in red), GMRT 323 MHz radio (in green) (Bonafede
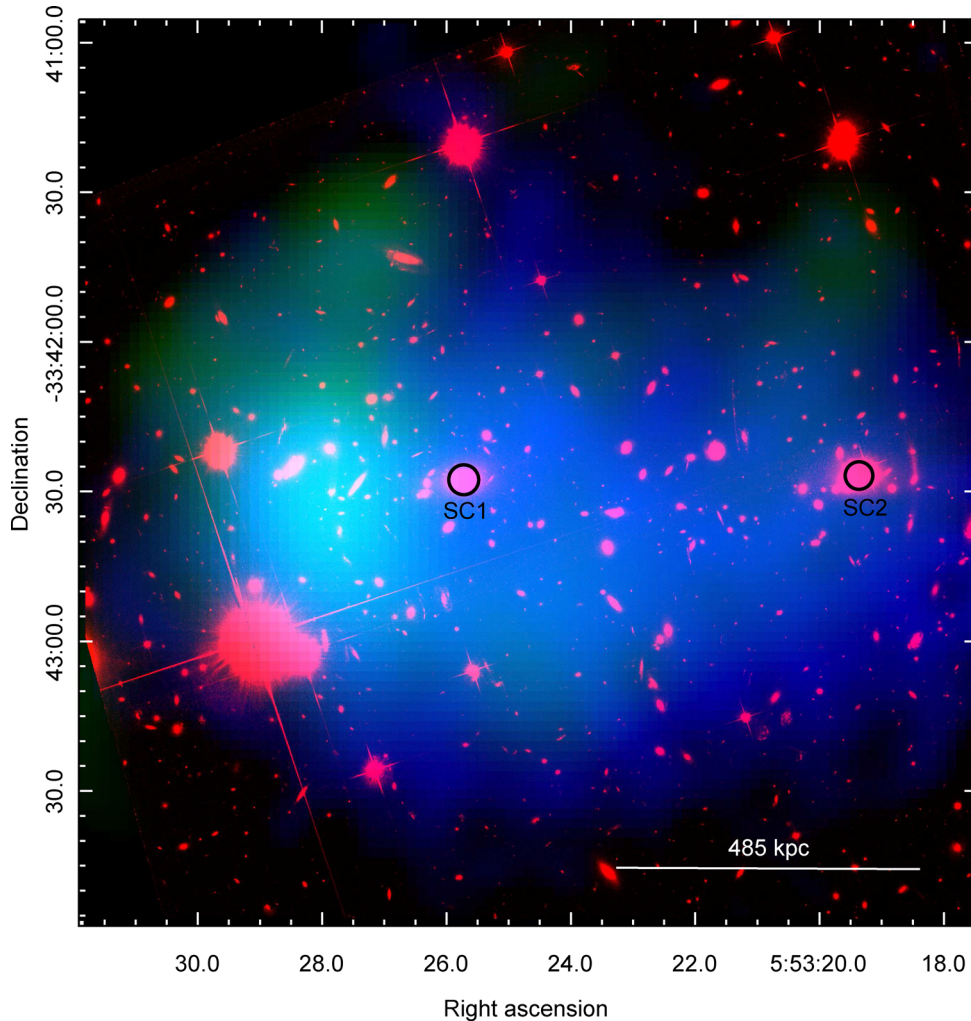
Figure 2. Tri-colour image of MACS J0553.4−3342 obtained using 0.7−4.0 keV *Chandra* X-ray data (shown in blue colour), *HST* optical *I*-band (F814W) data (red colour) and the GMRT 323 MHz data (green colour). This figure reveals the optical counterparts of the two subclusters (SC1 and SC2).

et al. 2012) and 0.7–4.0 keV *Chandra* X-ray image (in blue) observations. The resultant composite image is shown in Fig. 2.

In Fig. 3, the *HST* images of central 30×30 arcsec^2 $\sim$(250×250 kpc) regions centred around the brightest galaxies of possible subclusters SC0, SC1 and SC2 are shown from left to right. In these images, we find a compact subcluster of galaxies, dominated by a brightest cluster galaxy (BCG), in the heart of the X-ray halo SC1 at the centre of the system (Bonafede et al. 2012). In addition, we find another subcluster, $\sim$ 650 kpc away to the west of SC1, marked as SC2 in this figure, also falling within the diffuse X-ray emission, but not showing any bright X-ray peak [this subcluster is not mentioned in Bonafede et al. (2012).]. In Fig. 4, we show the *HST* F814W image of an extended 3.3×3.3 arcmin^2 region, where all galaxies with $18.5 < I < 27.0$ mag are marked with a red circle, enclosed by a further blue circle if their colour $V - I$ is in the range 1.0–1.25. The inner 30 arcsec of the subclusters SC1 and SC2 is also indicated.

### 3.2 Colour–magnitude diagram of the subclusters

It is well known that the early-type galaxies (ETGs; ellipticals and lenticulars) in clusters mostly lie in the core where the density of galaxies is higher, while the late-type (e.g. spirals) galax-

ies are predominant in the outskirts (e.g. Nantais et al. 2013; Macario et al. 2014). The CMDs show that the early-type members mostly appear along a well-defined *red sequence* (e.g. Holden et al. 2004; Gladders & Yee 2005; Mei et al. 2005; Postman et al. 2005; Stanford et al. 2005). The late-type galaxies scatter in such a plot with bluer colours, and the bimodal CMD provides a useful tool to examine the properties of the galaxy population of a massive cluster. In particular, in cases where redshifts for members are not widely available, the CMD provides a good way of identifying ETG member galaxies of clusters, and quantifying field contamination (e.g. Stanford, Eisenhardt & Dickinson 1998; Kodama & Bower 2001; De Lucia et al. 2007). However, this method becomes progressively uncertain for clusters at higher redshift.

As redshifts for each of the cluster member of MACS J0553.4−3342 are not available in the literature, here we construct the CMD for the MACS J0553.4−3342 field for finding the ETG membership of SC1 and SC2 by plotting the $(V - I)$ colours of the galaxies versus their *I*-band magnitudes from these *HST* observations, within $R_{500} = 1.5$ Mpc of the cluster centre (Fig. 5, left panel). We have selected only the extended sources in the field with flag=1 or concentration index CI >1.5. This plot clearly shows the *red sequence* of ETGs in the core of MACS J0553.4−3342, with the
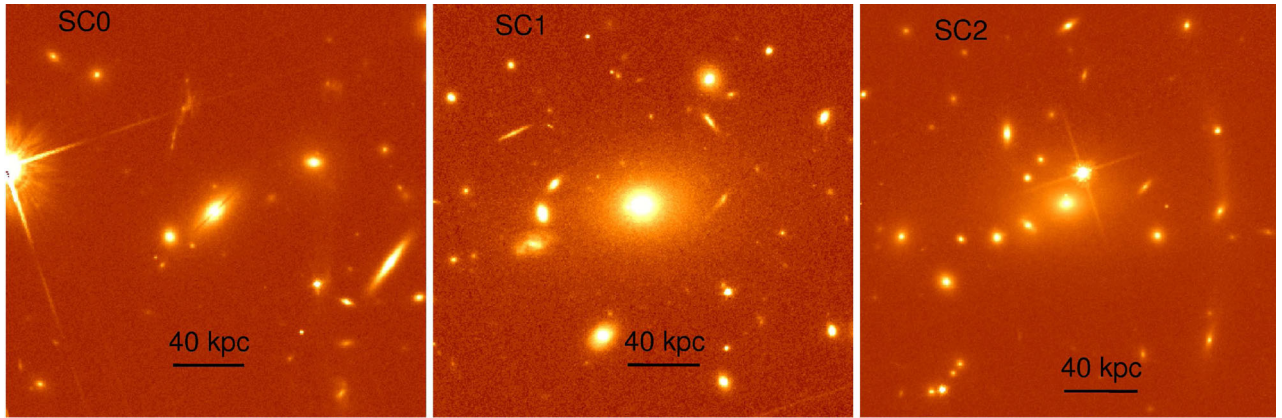
Figure 3. *HST I*-band (F814W) images of three regions of the MACS J0553.4−3342 system, centred on SC0, SC1 and SC2, respectively, each 30×30 arcsec^2 in size. A disc galaxy with a prominent dust lane dominates SC0.
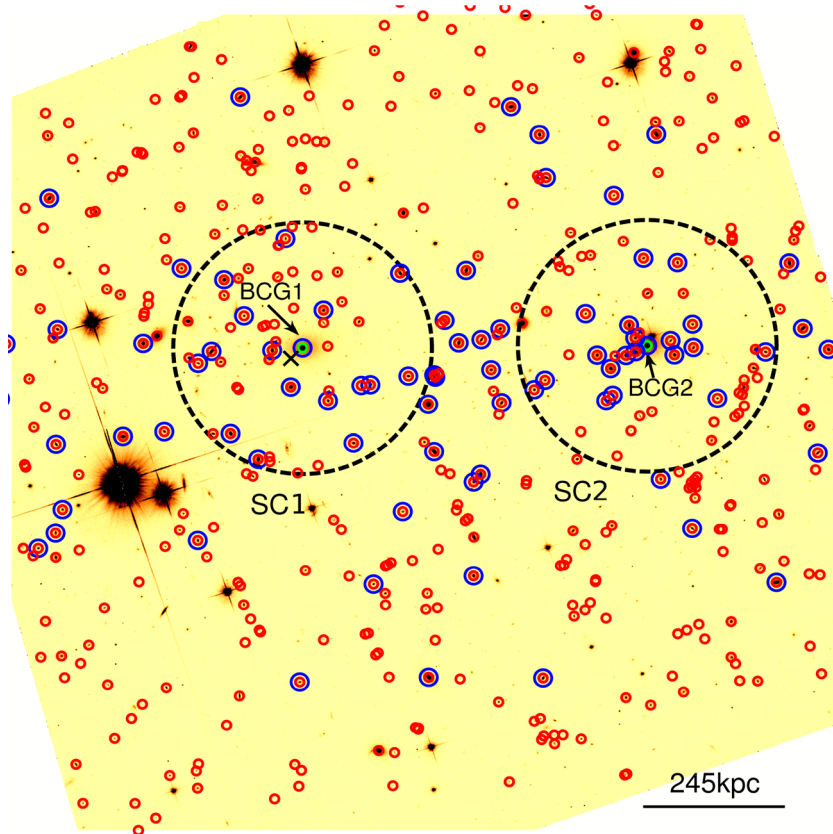

Figure 4. An *HST* image of (F814W) the central $\sim 3.3 \times 3.3$ arcmin^2 region of MACS J0553.4−3342. The subclusters SC1 and SC2 are indicated, and their BCGs and neighbouring members from the inner 30 arcsec are shown by black dotted circles. The red circles indicate the galaxies with *I*-band magnitude in the range of 18.5−27, while the blue circles mark the galaxies with $V - I$ colours in the range $V - I = 1.0 - 1.25$. The point 'x' indicates the position of the X-ray peak associated with the subcluster SC1.

I-band magnitudes in the range between 18.5 and 23.5 and the $V - I$ colour-cut between ~ 1 and 1.25. This CMD shows that nearly all the red galaxies with their $V - I$ colour values in this range are part of the same cluster. Interestingly, the BCGs associated with the subclusters SC1 and SC2, highlighted by black circles in Fig. 2, appear close to one another confirming their membership. Their position in CMD plane is also shown in Fig. 5 (left panel). It is also noted that nearly all the members within 30 arcsec of the BCGs (marked

by dotted black circles in Fig. 4) strictly follow the red sequence of the ETGs.

In Fig. 5 (right panel), the colour–magnitude information for all the member galaxies extracted from 30 arcsec circular region is highlighted by yellow filled circles for SC0, red filled triangles for SC1 and open blue circles for SC2. The 'subcluster' earlier identified as SC0, placed to the east of SC1 (Fig. 1), corresponds to a compact group of galaxies visible in the *HST* image, dominated by
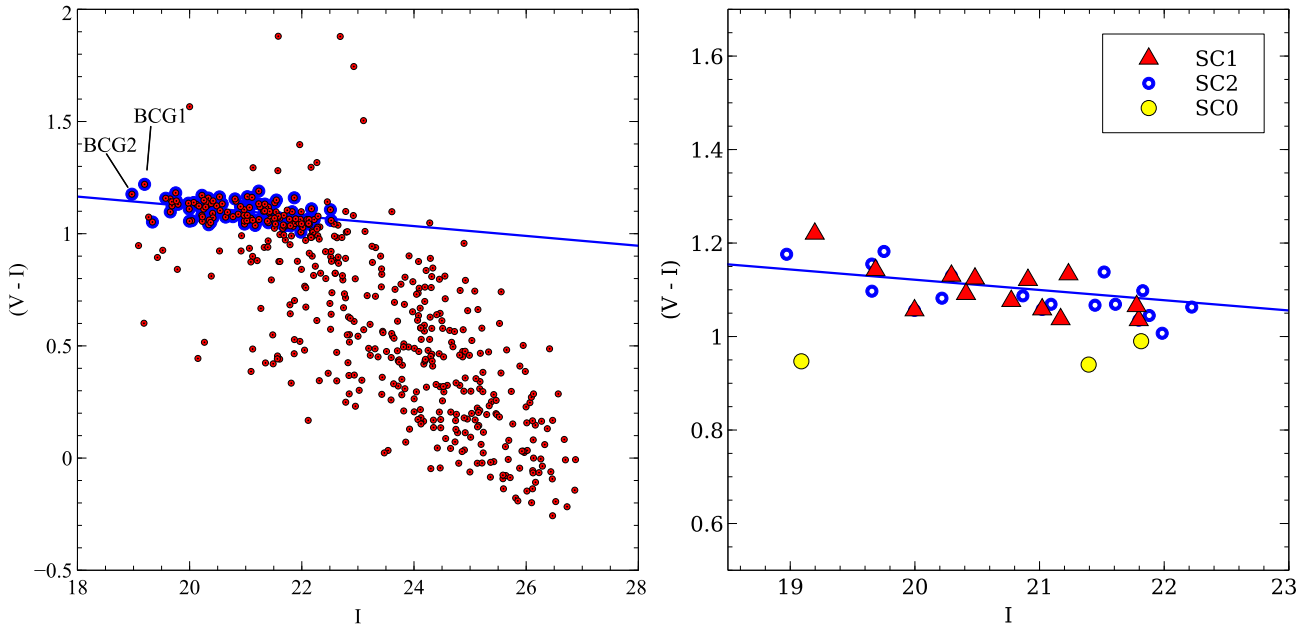
Figure 5. Left panel: the CMD for all the galaxies that have been identified from within the field by the Hubble-extended source catalogue (Whitmore 2015). The filled red circles show galaxies detected within the $\sim 3.3 \times 3.3$ arcmin^2 field of view around the centre of MACS J0553.4−3342, while the blue circles are the red-sequence galaxies within the colour range $V - I$=1.0-1.25. Right panel: a zoomed CMD of all galaxies within the central 30×30 arcsec^2 of SC0 (filled yellow circles), SC1 (red triangles) and SC2 (open blue circles). The CMD of SC0 indicates that the prominent galaxies in this subcluster are bluer in colour than the red sequence in SC1 and SC2, and therefore possibly closer to us.

an edge-on disc galaxy with a prominent dust lane. The I-band magnitudes of these galaxies are between 19.09 and 21.89 and their $V - I$ colour is in between 0.97 and 0.99 shown in Fig. 5 (right panel). The CMD clearly shows that these galaxies of SC0 lie significantly below the red sequence corresponding to the subclusters SC1 and SC2, and therefore the galaxy group SC0 cannot be at the same redshift as SC1 and SC2. Therefore, in the rest of this paper, we will consider this galaxy group to be a projected foreground system, and not part of the MACS J0553.4−3342 cluster. The bright X-ray peak near to SC0 has a high luminosity (0.5−10.0 keV) of $\sim 2.7 \times 10^{44}$ erg s^{-1} (for more detail, see Section 5.3) which could not have come from such a poor group of galaxies and is likely to be a part of MACS J0553.4−3342.

4 X-RAY SPATIAL AND SPECTRAL ANALYSIS

4.1 Surface brightness profiles

X-ray surface brightness profiles are crucial ingredients for the investigation of shocks and cold fronts, as indicators of the merging processes occurring on the scale of galaxy clusters (Ogrean et al. 2015; Botteon et al. 2016; Dasadia et al. 2016). To identify such features in the environment of MACS J0553.4−3342 we have derived azimuthally averaged surface brightness profiles of the X-ray emitting gas distribution in this cluster by extracting X-ray counts from within the circular annuli, with their centres as indicated in Fig. 6 (left panel). The extracted surface brightness profile was then fitted with the one-dimensional β-model following the χ^2 statistics of Gehrels (1986),

$$\Sigma(r) = \Sigma_0 \left[1 + \left(\frac{r}{r_0} \right)^2 \right]^{-3\beta + 0.5}, \qquad (1)$$

where $\Sigma(r)$ represents the X-ray flux at the projected distance r, Σ_0 the central surface brightness, r_0 the core radius and β the slope parameter of the profile. The best-fitting 1D β surface brightness profile is shown by the continuous line in Fig. 6 (right panel) with the best-fitting parameters β and r_0 being 0.78 and 304 kpc, respectively.

Unlike in the case of the cool-core clusters (Pandge et al. 2013; Sonkamble et al. 2015; Vagshette et al. 2017), the data points in the central region of this cluster lie below the best-fitting model. A comparison of the β-model and the data points reveals an edge or discontinuity at a radius of $\sim$40 arcsec. Another probable discontinuity is seen at $\sim$80 arcsec.

4.2 Global X-ray emission

To examine the global X-ray emission characteristics of the ICM in the environment of MACS J0553.4−3342, we have extracted a cumulative 0.7−8.0 keV spectrum, from a circular region of radius R_{500}=3.09 arcmin ($\sim$1500 kpc), as shown in Fig. 7 (yellow dotted circle). A corresponding background spectrum was also extracted from the normalized blank sky background file. The spectrum was then grouped to have at least $\sim$25 counts per spectral bin and was imported to XSPEC for further fitting using χ^2 statistics. We tried to constrain the spectrum with an absorbed single-temperature plasma model APEC (Smith et al. 2001), with the Galactic absorption fixed at $N_H^{\mathrm{Gal}} = 0.32 \times 10^{21}$ cm^{-2} (Dickey & Lockman 1990), letting all other parameters (e.g. temperature, metallicity and normalization) vary. The best-fitting minimum gives $\chi^2 = 364.15$ for 383 degrees of freedom (d.o.f.) with the elemental abundance 0.15$\pm$ 0.06 Z$_\odot$ and the ICM temperature amounting to 12.08$\pm$0.63 keV. This implies that MACS J0553.4−3342 represents one of the hottest merging clusters known to us. In the [0.1 − 2.4, keV] (*ROSAT*-like) band, the X-ray luminosity within the R_{500} region equals $L_{500,[0.1−2.4,\mathrm{keV}]} = 1.02 \pm 0.03 \times 10^{45}$ erg s^{-1}.
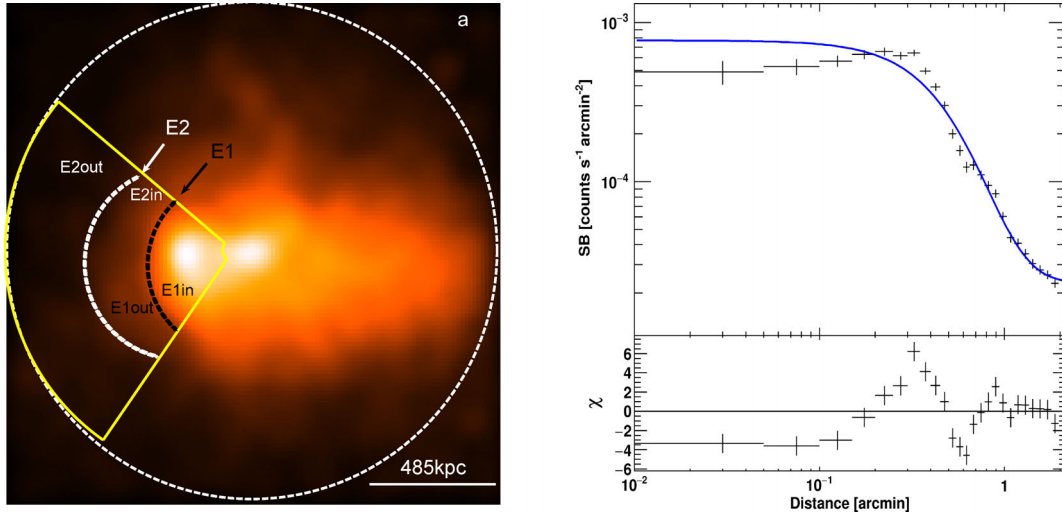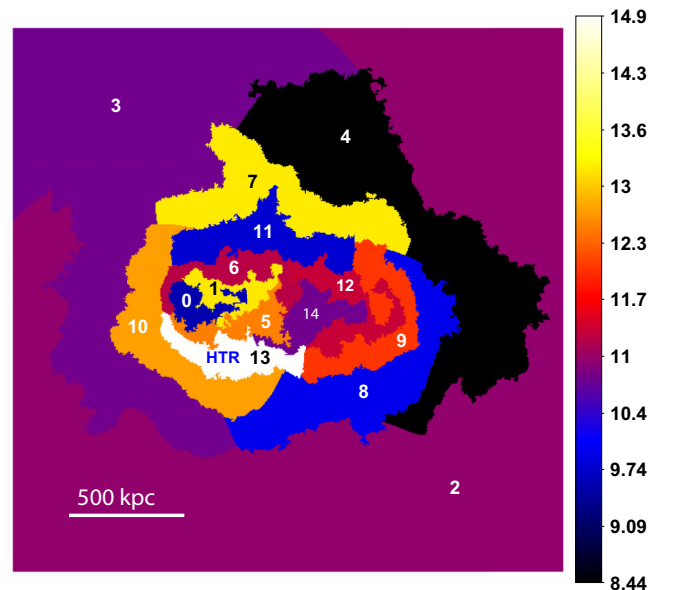
Figure 6. Left panel: the 0.7–4.0 keV *Chandra* image used for the extraction of the surface brightness profile of the distribution of the ICM within MACS J0553.4−3342. The highlighted wedge shaped arcs are for extracting profiles for the identification of the discontinuities in the surface brightness distribution. Right panel: projected radial surface brightness distribution in the energy range 0.7−4.0 keV of MACS J0553.4−3342. The continuous line in this figure indicates the best-fitting 1D β-model to the data points (black crosses).
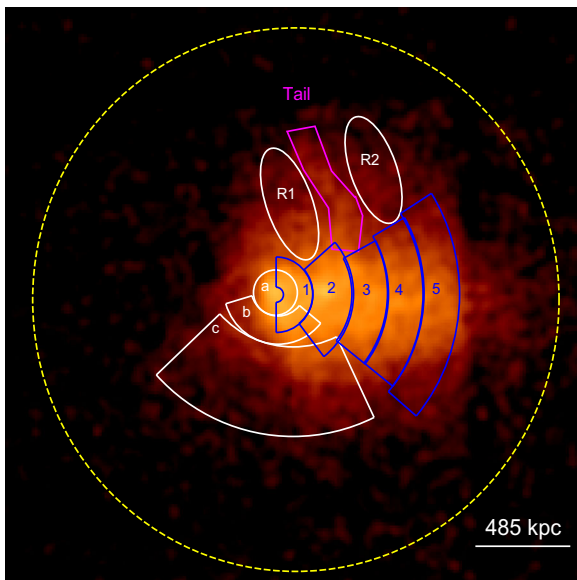
Figure 7. The *Chandra* image of MACS J0553.4−3342 (energy range of 0.7−7.0 keV), delineating different regions of interest used for spectral extraction. The image has been exposure-corrected, background-subtracted, and smoothed with a 3σ-wide Gaussian after the removal of point sources.

Figure 8. 2D temperature map of the ICM distribution within the central 5 × 5 arcmin^2 region of MACS J0553.4−3342. Temperature values of the gas from different regions marked in this figure are listed in Table 2. Note the temperature peak (shown as HTR) in arc 13.

4.3 Temperature map of the ICM

We have derived a two-dimensional temperature map of the hot ICM within MACS J0553.4−3342, following the 'contour binning' technique of Sanders (2006). This was achieved by generating a contour binned image of 15 different regions, with a minimum signal-to-noise ratio (S/N) of ∼40 (i.e. 1600 counts). The regions were constrained to the geometrical factors of 2 so that they would not be too elongated. Spectra and response files were extracted separately from individual bins. The spectra were then grouped to have at least 20 counts per energy bin and were fitted with an absorbed single-temperature APEC model as above. The best-fitting temperature values from this analysis are shown in the form of the temperature map (Fig. 8) and are also summarized in Table 2.

This map reveals that the ICM temperature varies substantially within the scale of the cluster, indicating its complex nature. In the same figure a high-temperature region (HTR; region 13) is indicated. Another jump in the temperature of the ICM is also evident along the east of this cold front and is probably due to the presence of a shock. Detailed properties of these cold and shock fronts are discussed below. Notice the complexity and extended nature of the ICM in the central region. It appears to be inhomogeneously extended along the east–west direction likely due to the interactions between the two subclusters SC1 and SC2.

It is possible that the cold and shock fronts exist along the south and west directions of the X-ray centre of the cluster. To look for them, we have extracted separate spectra from the regions a, b and

Table 2. Best-fitting spectral properties of the ICM extracted from 15 different regions of the 2D temperature map (Fig. 8).

Reg.	Net counts	χ^2 (d.o.f.)	kT (keV)	Norm (10^{-4}) (cm^{-3})
0	1940	79.01 (77)	9.57 ± 1.25	3.75 ± 0.14
1	1980	86.23 (80)	13.18 ± 1.98	3.80 ± 0.10
2	4866	122.92 (128)	11.0 ± 1.86	3.94 ± 0.13
3	3055	103.73 (120)	10.80 ± 1.69	3.30 ± 0.18
4	2354	100.99 (94)	8.44 ± 0.23	6.91 ± 0.36
5	1961	73.65 (76)	12.51 ± 1.83	3.56 ± 0.09
6	1990	66.79 (78)	11.24 ± 1.49	3.63 ± 0.14
7	1988	70.59 (79)	13.19 ± 2.36	3.27 ± 0.09
8	1987	74.75 (80)	9.96 ± 1.39	4.16 ± 0.11
9	2083	92.20 (83)	12.04 ± 1.80	3.62 ± 0.17
10	1979	76.50 (80)	12.71 ± 2.14	3.45 ± 0.10
11	1957	63.37 (80)	9.78 ± 1.72	3.43 ± 0.13
12	1960	102.52 (78)	11.35 ± 1.30	3.95 ± 0.19
13	1945	72.41 (78)	14.94 ± 2.13	3.45 ± 0.17
14	1936	68.00 (76)	10.78 ± 1.70	3.41 ± 0.14

c (white semicircular arcs in Fig. 7) and regions 1, 2, 3, 4 and 5 (blue arcs in Fig. 7). The extracted spectra were treated with an absorbed single-temperature plasma code APEC with the absorption fixed at the Galactic value and the abundance at $Z = 0.20\ Z_\odot$. The best-fitting thermodynamical parameters temperature (kT), electron density (n_e), pressure (P) and the entropy ($S = kT \times n_e^{-2/3}$) for different regions are shown in Fig. 9 and are also tabulated in Table 3. The entropy, the key parameter that records gain of the thermal energy through the shocks and/or AGN feedback while remaining insensitive to the adiabatic compressions and expansions, exhibits a significant increase, while moving from region 1 through 5 (Fig. 9, left panel). Similar rise in the entropy is also evident in the regions a, b and c (Fig. 9, right panel). This analysis failed to detect any compression due to the presence of shocks and fronts. Similar results were also found in the surface brightness analysis along these regions.
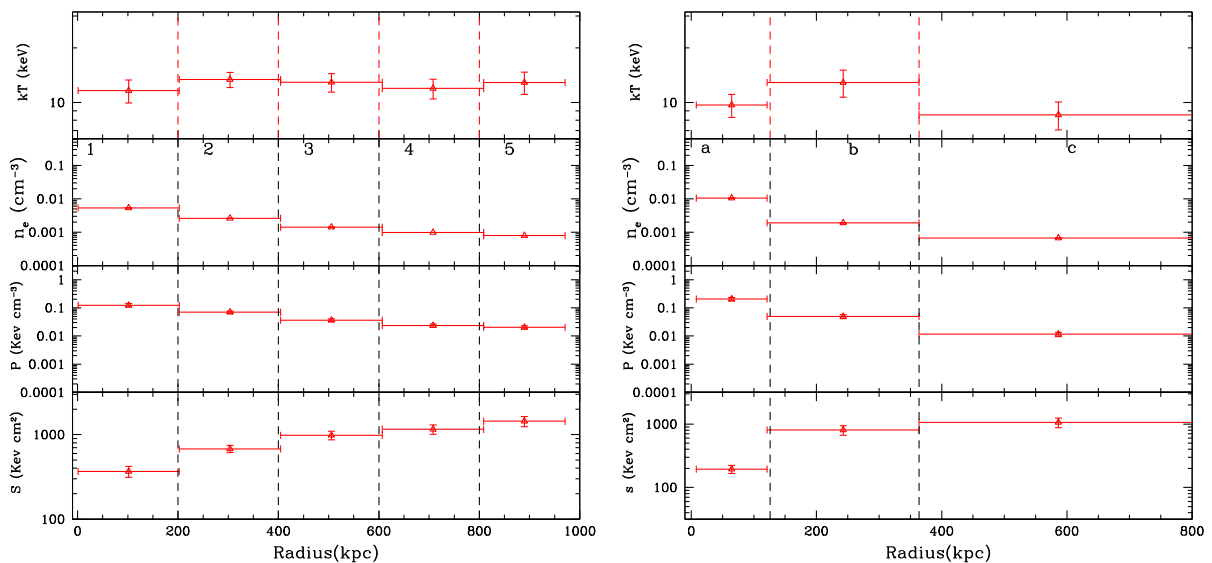
4.4 X-ray tail

The *Chandra* image of the cluster MACS J0553.4−3342 (Fig. 1) has also revealed a prominent tail-like structure that extends in the north-east direction of the subcluster SC1 up to a distance of about 130 arcsec ($\sim 1002\ kpc$) (at 2σ). This might be the longest tail, originating from a stripping process, ever observed in the cluster environment. To examine the thermal properties of the ICM in this tail-like structure, we analysed the spectra extracted from the long magenta polygon and its neighbouring regions R1 and R2 (white ellipses), as shown in Fig. 7. The extracted spectra were independently fitted with an absorbed single-temperature APEC model, with the abundance fixed at 0.2 $Z_\odot$. The best-fitting temperature values of the gas appearing in the tail region and its neighbouring regions R1 and R2 are tabulated in Table 4, and are found to be equal to $11.86 \pm 2.3\ keV$, $13.21 \pm 4.9\ keV$ and $13.96 \pm 5.6\ keV$, respectively. The comparison of these values reveals that the gas extending in the form of the X-ray tail is similar to the regions R1 and R2 within the uncertainties, implying that it has emerged in the form of a compressed ram-pressure striped tail during the major merging process that happened in the cluster. Such a release of gas in the form of luminous tail is possible as an outcome of the merger of two equally massive subclusters (Reiprich et al. 2004; Eckert et al. 2014; Schellenberger & Reiprich 2015).

5 DISCUSSION

5.1 Surface brightness edges

The surface brightness distribution of the ICM in Fig. 1 clearly shows an edge (E1) at ~ 40 arcsec on the east of the X-ray centre of the cluster MACS J0553.4−3342 (SC1). This was also evident in the radial surface brightness profile derived above. The radial profile also indicated the presence of another edge or discontinuity (E2) at ~ 80 arcsec beyond SC1. To confirm the presence and to examine the significance of these edges relative to the neighbouring regions, we have extracted two separate surface brightness profiles of the X-ray emission from the regions close to E1 and E2. The

Figure 9. Profiles of the thermodynamical parameters temperature (kT), electron density (n_e), pressure (P) and entropy (S) (respectively from top to bottom) for the extracted spectra from regions 1, 2, 3, 4, and 5 are shown in the left panel, while those for regions a, b and c are shown in the right panel.

Table 3. Best-fitting thermodynamical parameters (temperature, electron density, pressure, entropy) of the ICM extracted from different regions in Fig. 7.

Reg.	kT (keV)	n_e (10^{-3}cm^{-3})	P (keVcm^{-3})	S (keVcm^2)
1	11.63 ± 1.20	5.34 ± 0.06	0.12 ± 0.018	367 ± 57
2	13.39 ± 1.20	2.60 ± 0.01	0.069 ± 0.006	679 ± 65
3	12.93 ± 1.50	1.41 ± 0.01	0.036 ± 0.006	984 ± 114
4	11.96 ± 1.00	0.98 ± 0.01	0.023 ± 0.004	1156 ± 145
5	12.90 ± 1.80	0.78 ± 0.01	0.020 ± 0.003	1440 ± 200
a	9.68 ± 1.29	10.5 ± 0.01	0.21 ± 0.003	194 ± 28
b	12.91 ± 2.20	1.19 ± 0.01	0.050 ± 0.022	804 ± 137
c	8.56 ± 1.50	0.67 ± 0.01	0.018 ± 0.004	1060 ± 185

Table 4. Best-fitting parameters of the X-ray tail and its neighbouring regions.

Regions	Counts	kT (keV)	Z (fixed) ($Z_\odot$)	$L_{[0.1-2.4,\mathrm{keV}]}$ 10^{43}ergs^{-1}	χ^2 (d.o.f.)
Tail	3171	11.86 ± 2.3	0.2	6.90 ± 0.10	103.37 (111)
R1	1006	13.21 ± 4.9	0.2	1.16 ± 0.06	35.65 (42)
R2	1050	13.96 ± 5.6	0.2	1.41±0.10	35.76 (47)

wedge shaped regions selected for this extraction have the opening angles of $130° - 240°$ and are shown in Fig. 6 (left panel).

The extracted surface brightness profiles in the energy range 0.7–4.0 keV are shown in Fig. 10 (left and right panels), corresponding to the edges E1 and E2, respectively. These figures clearly indicate a sharp discontinuity near the inner edge E1 (Fig. 10, left panel), while that near the outer edge E2 is marginally indicative (Fig. 10, right panel). To compute the compression parameters, and hence the Mach numbers corresponding to the ICM compression at these edges, we fitted these profiles with deprojected broken power-law density models, using the PROFFIT (V 1.4) package of Eckert, Molendi & Paltani (2011). These best-fitting broken power-law density models are represented by the continuous lines in the insets of both the figures and are parametrized as:

$$n(r) = \begin{cases} \mathcal{C}n_0 \left(\frac{r}{r_{\rm sh}}\right)^{-\alpha 1}, & \text{if } r < r_{\rm sh} \\ n_0 \left(\frac{r}{r_{\rm sh}}\right)^{-\alpha 2}, & \text{if } r > r_{\rm sh} \end{cases}, \quad (2)$$

where $n(r)$ represents the electron number density at distance r, n_0 the density normalization, C the density compression factor of the shock, α_1 and α_2 the power-law indices, while $r_{\rm sh}$ represents the radius corresponding to the putative edge or cold/shock front. We allowed all the parameters to vary during the fit. The best-fitting parameters yielded by fitting the broken power-law density model are listed in Table 5.

According to the Rankine–Hugoniot relations (Landau & Lifshitz 1959), the density compression factor C at the location of the compression is related to the Mach number $\mathcal{M}$ as

$$\mathcal{M} = \left[\frac{2C}{\gamma + 1 - C(\gamma - 1)}\right]^{1/2}. \quad (3)$$

Here, γ is the adiabatic index of the gas and we assume $\gamma = 5/3$ for the present case. Thus, for determining the Mach numbers at the location of compressions, we are required to estimate the temperature values and hence density of the gas on either sides of the edges. This was done by extracting separate spectra from the inner and outer sides of the surface brightness edges, e.g. E1$_{\rm in}$ and E1$_{\rm out}$

for E1 and E2$_{\rm in}$ and E2$_{\rm out}$ for E2. All the four spectra were then fitted independently with a single-temperature APEC model with the redshift fixed at 0.43. The best-fitting temperature values of the ICM across the edge E1 are 9.49 ± 1.12 keV (T_1) and 15.34 ± 2.04 keV (T_2) at E1$_{\rm in}$ and E1$_{\rm out}$, respectively. Here, the gas on the inner side of the edge E1 appears denser and exhibits a sharp boundary, probably due to the presence of a merger-driven cold front. The measured values of the ICM pressures on either side are the same within the uncertainties, thereby confirming that the edge E1 is formed by a merger-driven cold front. Similarly, we also compute the best-fitting temperature values of the ICM across the edge E2 and are found to be equal to 15.34±2.04 keV and 8.80±1.84 keV for E2$_{\rm in}$ and E2$_{\rm out}$, respectively. Then we compute the corresponding Mach numbers using the relation (Landau & Lifshitz 1959)

$$\mathcal{M} = \frac{\left(8\frac{T_2}{T_1} - 7\right) + \left[\left(8\frac{T_2}{T_1} - 7\right)^2 + 15\right]^{1/2}}{5}. \quad (4)$$

The Mach numbers $\mathcal{M}$ computed using equations (3) and (4) at the edge E2 are 1.33 ± 0.11 and 1.72 ± 0.36, respectively. These estimates along with the measured values of the ICM temperatures collectively indicate that this edge E2 is due to a shock front. A shock front ahead of the merger-driven cold front in this system is very similar to those observed in the *Bullet cluster* (Markevitch et al. 2002) and the *Toothbrush cluster* (van Weeren et al. 2016), justifying this renewed interest in this cluster.

5.2 The morphological planes

We have already seen that the cluster MACS J0553.4−3342 represents a highly disturbed, merging system. The *Chandra* image (Fig. 1) confirms that the large-scale X-ray emission associated with this cluster appears to be elongated towards the west. Further, the *HST I*-band image reveals two close subclusters SC1 and SC2 separated by about ∼107.5 arcsec (∼650 kpc), pointing towards an ongoing merging process. Therefore, it is of great interest to compare the dynamical state of MACS J0553.4−3342 with other clusters that represent different stages of their dynamical phases ranging from the highly disturbed systems to the most relaxed ones.

For this purpose, we have made use of the three non-parametric morphology parameters *Gini*, M_{20} and Concentration index (C) to characterize the degree of disturbances in these clusters (Parekh et al. 2015), found to be useful in characterizing galaxy clusters according to their level of dynamical disturbance. The *Gini* coefficient parametrizes the flux distribution among the image pixels, such that for the relaxed and cool-core clusters, where the X-ray flux is concentrated only in a small number of image pixels, its value is closer to 1, while in non-relaxed clusters, where the flux is more widely distributed among the image pixels, *Gini* takes values close to 0 (e.g. Lotz, Primack & Madau 2004). The moment of light M_{20} is the normalized second-order moment of relative contribution of the brightest 20 per cent pixels (Lotz et al. 2004) and is a measure of the spatial distribution of the bright cores and subclusters in the cluster. Typically, the value of the moment of light parameter M_{20} is found to vary in the range between −2.5 for the case of relaxed clusters and −0.7 for most disturbed systems. The third parameter C is a measure of the concentration of the flux in the cluster and depends on the ratio of the radii at which 80 per cent and 20 per cent of the cluster fluxes are measured (Conselice 2003). It takes the minimum value of 0.0 for the most disturbed clusters.

For estimating these morphological parameters in the case of MACS J0553.4−3342 we have made use of the cleaned, background
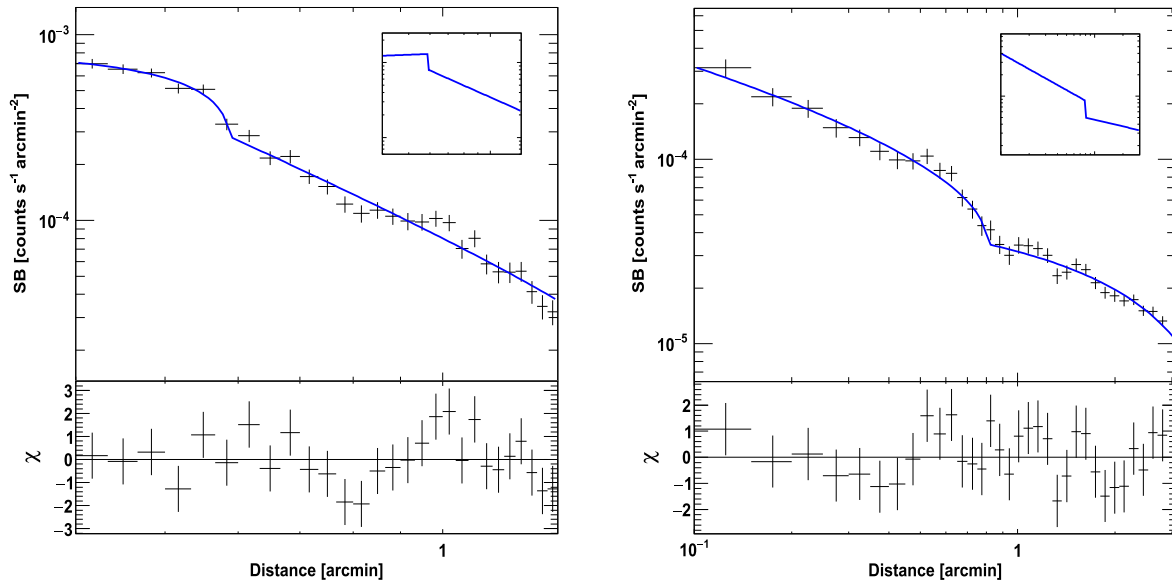
Figure 10. Projected surface brightness profile extracted from the wedge shaped sector with opening angles between 130° and 240° around the region indicated by E1 (left panel), while that around the edge E2 is shown in right panel. Both of these profiles were fitted with the deprojected broken power-law density model whose 3D simulations are shown in the insets. Note the jumps in the surface brightness near both the edges E1 and E2.

Table 5. Parameters obtained from the best-fitting broken power-law density model.

Regions	α_1	α_2	r_{sh} (arcmin)	n_0 (10^{-4}cm^{-3})	C	χ^2/d.o.f.	Mach no. ($\mathcal{M}$)
E1	0.58 ± 0.08	1.68 ± 0.13	0.65 ± 0.02	7.59 ± 0.30	1.60 ± 0.10	29.17/21.00	−
E2	1.23 ± 0.18	0.56 ± 0.05	1.29 ± 0.04	0.30 ± 0.04	1.45 ± 0.16	48.96/48	1.33 ± 0.11

and exposure-corrected *Chandra* image. The computed parameters from within the 500 kpc region around the cluster centroid in this figure are listed in Table 6. To compare the dynamical state of MACS J0553.4−3342 with those for the sample clusters of Parekh et al. (2015), we plot different correlations among the morphological parameters and are known as the *morphological planes* (Fig. 11). The control sample comprises 49 low-redshift ($z = 0.2$–0.3) and 36 high-redshift ($z = 0.3$–0.8) clusters of different dynamical states, representing relaxed as well as disturbed phases. Open circles in this figure represent the most relaxed clusters, diamonds the relaxed, pluses '+' the non-relaxed and the crosses 'x' the most disturbed systems from the sample. The squares in all three plots represent the galaxy clusters with radio haloes, known to be merging clusters and are taken from Giovannini et al. (2009). This figure reveals that the relaxed and disturbed systems take positions on extreme ends, while the clusters with intermediate dynamical stages occupy positions in between them. These plots segregate clusters using different combinations of the morphological parameters with their limits ranging between $-0.65 < G < 0.40$, $-1.4 < M_{20} < -2.0$ and $1.55 < C < 1.0$. We show the position of MACS J0553.4−3342 in these plots with the green star using its morphological parameters

given in Table 6. Careful observations of all these plots reveal that MACS J0553.4−3342 occupies position in the family of the highly non-relaxed clusters.

We have also plotted the morphological parameters of the control sample including the radio-halo merging clusters of Giovannini et al. (2009) as a function of the cluster temperature and the resultant plots are shown in Fig. 12. For a better representation we have divided these plots in three different regions: (1) the systems of dynamically relaxed nature, (2) radio-quiet merging clusters, i.e. mergers without radio haloes and (3) the radio-loud merging clusters (i.e. clusters with radio haloes) with ICM temperature $T > 6$ keV. In these plots we also indicate the position of MACS J0553.4−3342 by a green star. In all the three plots MACS J0553.4−3342 occupies position in region 3, indicating that it belongs to the class of galaxy clusters that are dominated by the non-relaxed dynamical state with radio haloes around them. MACS J0553.4−3342 has also been reported to be the hottest galaxy clusters with a 1.3 Mpc-scale radio halo (Bonafede et al. 2012). In these plots we also indicate, by a square surrounded by a green circle, the well-known highly disturbed, extremely hot galaxy cluster 1E 0657-56 (The 'Bullet Cluster') with a radio halo (Markevitch et al. 2002; Shimwell et al. 2014). Interestingly, MACS J0553.4−3342 appears close to this highly disturbed system in all the three plots (Fig. 12). In view of its similarity with the heavily disturbed systems, it is of great interest to obtain the detailed gravitational lensing mass map of the DM distribution in this cluster and compare its distribution relative to the baryonic and galactic components (Ebeling, Qi & Richard 2017). In short, our subcluster analysis clearly demonstrates that MACS J0553.4−3342 is a dynamically disturbed cluster, belonging to region 3, the region

Table 6. Morphology parameters for MACS J0553.4−3342 as discussed in Section 5.2.

Cluster	*Gini*	M_{20}	*Concentration*
MACS J0553.4−3342	0.40 ± 0.0023	-1.09 ± 0.30	0.85 ± 0.37
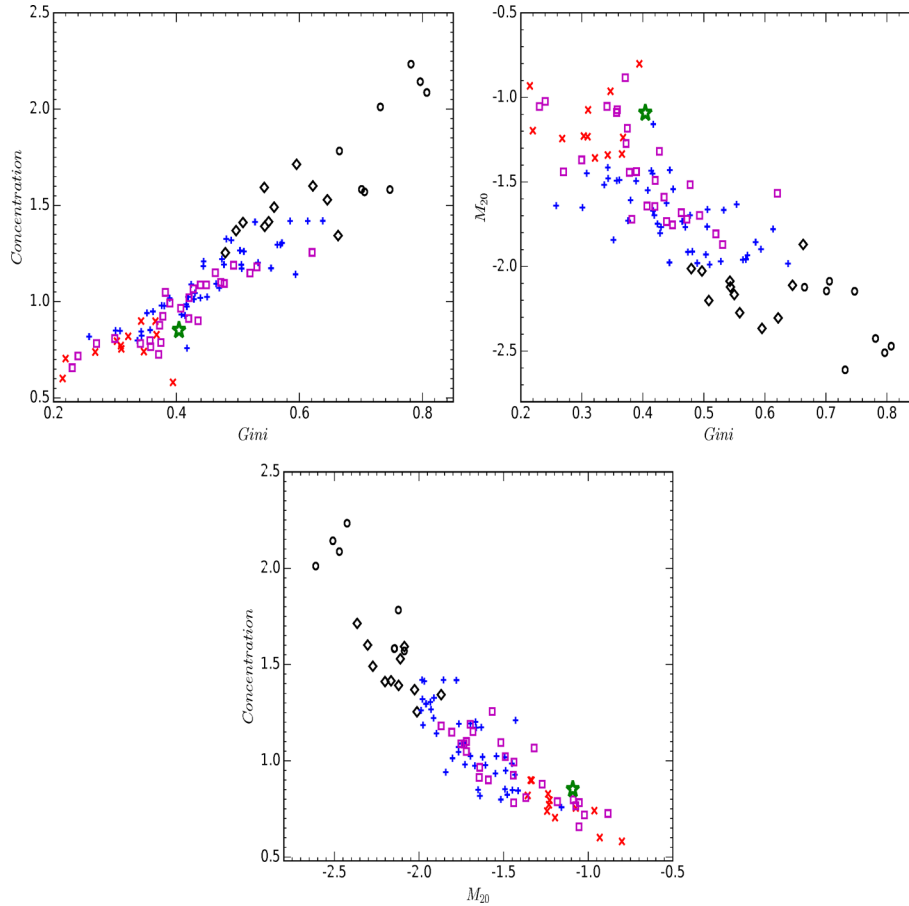
Figure 11. The morphological parameter planes for the control sample of galaxy clusters taken from Parekh et al. (2015) for identifying their dynamical states. Open circles in all the three plots represent the 'most relaxed' clusters, diamonds the 'relaxed' clusters, pluses the 'non-relaxed', while the 'most disturbed' clusters are indicated by crosses. The squares are clusters with radio haloes and known to be merging clusters. The position of MACS J0553.4−3342 in these plots is indicated by a green star (Giovannini et al. 2009).
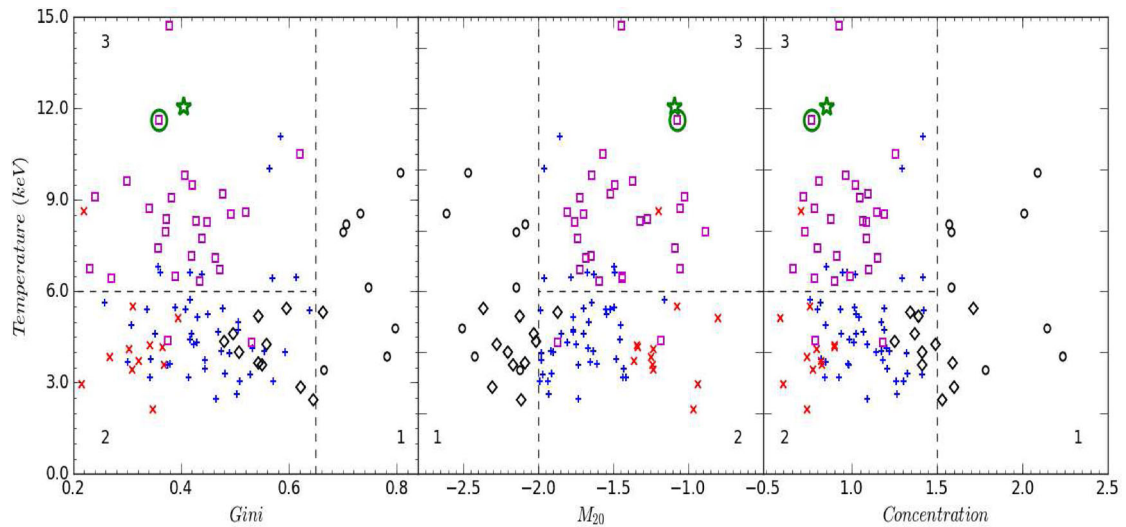
Figure 12. Morphology parameters versus temperature for the sample clusters as in Fig. 11. We subdivided the morphology parameter versus temperature plot into three regions: (1) dynamically relaxed clusters, (2) radio-quiet (no radio halo) merger clusters and (3) radio-loud (with radio halo) merger clusters. The green star represents MACS J0553.4−3342 while a square within a green circle shows the 'Bullet Cluster' 1E 0657−56.

dominated by the clusters exhibiting merging processes and radio haloes around them.

5.3 The nature of the X-ray bright peak east to the SC1

A bright X-ray peak is apparent about ∼200 kpc east of the eastern subcluster SC1. From our spectral analysis from X-ray photons extracted from an ∼15 arcsec (∼120 kpc) circular region of this peak, fitted in the same way as discussed in Section 4.2, the best-fitting temperature and (0.5−10.0 keV) band luminosity values are found to be 9.54±1.44 keV and ∼2.7 ± 0.10 × 10^{44}ergs^{-1} (minimum χ^2 = 122.74 for 96 d.o.f.). Comparing with the SC1 gas temperature, it is evident that the gas temperature in this X-ray bright peak is cooler than that of SC1 (see region 2 in Table 3 13.39 ± 1.20). This might be attributed to being due to the displacement of the cool dense gas from the eastern subcluster SC1 during the major merger event.

6 CONCLUSIONS

In this paper, we have presented the analysis of a total of 83 ks of *Chandra* X-ray observations, along with *HST* optical observations, of MACS J0553.4−3342, one of the hottest systems known representing a merging cluster. The main objectives of the study were to identify and confirm the presence of different subclusters in the environment of MACS J0553.4−3342, and also to investigate discontinuities or edges in the X-ray surface brightness distribution that remained undetected in the previous studies. The present study has clearly demonstrated that the ICM in this cluster hosts two merging subclusters, whose merger axis lies along the east–west direction of the cluster. Important results from this study are summarized below.

(i) Optical identification of the member galaxies in the field of MACS J0553.4−3342 cluster confirms that this system actually hosts two different merging subclusters SC1 and SC2 separated by a projected distance of ∼650 kpc.

(ii) The exposure-corrected background-subtracted image shows an X-ray tail-like structure extending up to a projected distance of 130 arcsec or ∼1002 kpc (at 2σ confidence) from the centre of SC1. The gas along this tail appears to be similar to its neighbouring region within the uncertainties.

(iii) X-ray surface brightness profiles extracted from the wedge shaped regions with opening angles of 130° − 240° indicate two sharp surface brightness edges (E1 and E2) at ∼40 arcsec (∼323 kpc) and ∼80 arcsec (∼647 kpc) east of the centre of the cluster, respectively. The inner edge E1 represents a merger-driven cold front, while the outer edge E2 is due to a shock front. The Mach numbers $\mathcal{M}$ associated with the compression due to the shock at E2 are estimated to be 1.33 ± 0.11 and 1.72 ± 0.36, from a density compression jump analysis and from the temperature measurement on either sides of the shock front. A shock front ahead of the merger-driven cold front is very similar to those seen in the *Bullet* and the *Toothbrush* clusters.

(iv) Spectral studies reveal the ICM in MACS J0553.4−3342 to be at an average temperature of T_{500}= 12.08 ± 0.63keV, with average metallicity of Z_{500} = 0.15±0.06 $Z_\odot$ and luminosity $L_{500, [0.1 − 2.4keV]}$ =1.02±0.03 × 10^{45} ergs^{-1}. This makes it one of the hottest and brightest clusters known.

(v) The dynamical state of MACS J0553.4−3342 is examined using the morphological parameters as well as a subcluster analysis. This indicates that MACS J0553.4−3342 represents a case of a dynamically disturbed cluster.

(vi) The CMD plotted for MACS J0553.4−3342 demonstrates that nearly all the ETGs, including BCGs at SC1 and SC2, within 30 arcsec of the centres of the subclusters SC1 and SC2 are part of the same system, and lie within its well-defined red sequence.

REFERENCES

Arnaud K. A., 1996, in Jacoby G. H., Barnes J., eds, ASP Conf. Ser. Vol. 101, Astronomical Data Analysis Software and Systems V, Astron. Soc. Pac., San Francisco, p. 17
Bagchi J., Enßlin T. A., Miniati F., Stalin C. S., Singh M., Raychaudhury S., Humeshkar N. B., 2002, New Astron., 7, 249
Bagchi J., Durret F., Neto G. B. L., Paul S., 2006, Science, 314, 791
Bagchi J. et al., 2011, ApJ, 736, L8
Bonafede A. et al., 2012, MNRAS, 426, 40
Botteon A., Gastaldello F., Brunetti G., Dallacasa D., 2016, MNRAS, 460, L84
Conselice C. J., 2003, ApJS, 147, 1
Dasadia S. et al., 2016, MNRAS, 458, 681
De Lucia G. et al., 2007, MNRAS, 374, 809
Dickey J. M., Lockman F. J., 1990, ARA&A, 28, 215
Ebeling H., Qi J., Richard J., 2017, MNRAS, 471, 3305
Eckert D., Molendi S., Paltani S., 2011, A&A, 526, A79
Eckert D. et al., 2014, A&A, 570, A119
Feretti L., Giovannini G., Govoni F., Murgia M., 2012, A&AR, 20, 54
Gehrels N., 1986, ApJ, 303, 336
Giovannini G., Bonafede A., Feretti L., Govoni F., Murgia M., Ferrari F., Monti G., 2009, A&A, 507, 1257
Gladders M. D., Yee H. K. C., 2005, VizieR Online Data Catalog, 215, 70001
Holden B. P., Stanford S. A., Eisenhardt P., Dickinson M., 2004, AJ, 127, 2484
Kodama T., Bower R. G., 2001, MNRAS, 321, 18
Landau L. D., Lifshitz E. M., 1959, Fluid Mechanics
Lotz J. M., Primack J., Madau P., 2004, AJ, 128, 163

Macario G. et al., 2014, A&A, 565, A13

Mann A. W., Ebeling H., 2012, MNRAS, 420, 2120

Markevitch M., Vikhlinin A., 2007, Phys. Rep., 443, 1

Markevitch M., Gonzalez A. H., David L., Vikhlinin A., Murray S., Forman W., Jones C., Tucker W., 2002, ApJ, 567, L27

Mei S. et al., 2005, ApJ, 625, 121

Nantais J. B., Flores H., Demarco R., Lidman C., Rosati P., Jee M. J., 2013, A&A, 556, C4

Ogrean G. A. et al., 2015, ApJ, 812, 153

Pandge M. B., Vagshette N. D., Sonkamble S. S., Patil M. K., 2013, Ap&SS, 345, 183

Parekh V., van der Heyden K., Ferrari C., Angus G., Holwerda B., 2015, A&A, 575, A127

Plagge T. et al., 2010, ApJ, 716, 1118

Postman M. et al., 2005, ApJ, 623, 721

Randall S. W., Markevitch M., Clowe D., Gonzalez A. H., Bradač M., 2008, ApJ, 679, 1173

Reiprich T. H., Sarazin C. L., Kempner J. C., Tittley E., 2004, ApJ, 608, 179

Sanders J. S., 2006, MNRAS, 371, 829

Schellenberger G., Reiprich T. H., 2015, A&A, 583, L2

Shimwell T. W., Brown S., Feain I. J., Feretti L., Gaensler B. M., Lage C., 2014, MNRAS, 440, 2901

Smith R. K., Brickhouse N. S., Liedahl D. A., Raymond J. C., 2001, ApJ, 556, L91

Sonkamble S. S., Vagshette N. D., Pawar P. K., Patil M. K., 2015, Ap&SS, 359, 21

Stanford S. A., Eisenhardt P. R., Dickinson M., 1998, ApJ, 492, 461

Stanford S. A. et al., 2005, ApJ, 634, L129

Vagshette N. D., Naik S., Patil M. K., Sonkamble S. S., 2017, MNRAS, 466, 2054

van Weeren R. J. et al., 2009, A&A, 506, 1083

van Weeren R. J. et al., 2016, ApJ, 818, 204

Whitmore B., 2015, IAU General Assembly, 22, 2247054

ZuHone J. A., Kunz M. W., Markevitch M., Stone J. M., Biffi V., 2015, ApJ, 798, 90

This paper has been typeset from a TEX/LATEX file prepared by the author.